The impact of the operating field strength on the lasing properties of GaAs/(Al,Ga)As quantum-cascade lasers

L. Schrottke,[a] M. Giehler, R. Hey, and H. T. Grahn
Paul-Drude-Institut für Festkörperelektronik, Hausvogteiplatz 5-7, 10117 Berlin, Germany

(Received 31 January 2006; accepted 13 June 2006; published online 6 September 2006)

The gain coefficient of several GaAs/$Al_xGa_{1-x}As$ quantum-cascade lasers (QCLs) with a nominal Al content of $x=0.45$ has been calculated as a function of transition energy and electric field strength. We solve the Schrödinger and Poisson equations self-consistently in the framework of a linear scattering-rate model with periodic boundary conditions. The actual layer thicknesses as well as the Al content of the barriers have been obtained from x-ray diffraction. The calculated gain characteristics exhibit a large range of transition energies and a corresponding range of possible operating field strengths. These results may provide an explanation for the observation of a rather large range of the lasing energies for QCLs with nominally identical cascade structures. The comparison with the experimental values of the lasing energy reveals that most of the lasers operate below the designed field strength. The analysis of the operating field strengths and the threshold current densities indicates larger losses for higher field strengths probably due to leakage currents.
 [DOI: 10.1063/1.2335772]

I. INTRODUCTION

The application of quantum-cascade lasers (QCLs), which are promising light sources in the wavelength range from midinfrared[1] to terahertz radiation,[2] poses still a challenge insofar as the threshold current densities, in particular, for GaAs/(Al,Ga)As QCLs, are quite large. Furthermore, the lasing energies scatter considerably around the designed values, although the lasing energy for the individual QCLs does not significantly shift, when the applied voltage is varied. Recently, Giehler *et al.*[3] have shown that GaAs/(Al,Ga)As QCLs with a nominally identical cascade structure, but with different sheet doping densities in the injector between 3.5×10^{11} and 1.0×10^{12} cm^{-2} exhibit lasing energies with a variation of more than 20 meV. This rather large range can neither be explained by fluctuations of the layer thicknesses nor by a splitting of the laser level due to its coupling with the injector state as conjectured in an earlier study of GaAs/$Al_{0.33}Ga_{0.67}As$ QCLs.[4] In a subsequent investigation of GaAs/$Al_{0.45}Ga_{0.55}As$ QCLs,[5] we did not find such a splitting, although the lasing energies of the corresponding QCLs varied in a similar range.

In order to lower the threshold current densities of QCLs, there have been several attempts to modify the subband structure of the devices, i.e., the internal design, and to improve the resonator quality as well as the heat management, i.e., the external properties. In this paper, we focus on the internal processes rather than discussing the enormous progress of the device technology. After the design and preparation of the GaAs/$Al_{0.33}Ga_{0.67}As$ QCLs by Sirtori *et al.*,[6] in particular, after introducing plasmon-assisted waveguides,[7] significant progress has been achieved by Page *et al.*[8] using higher barriers, i.e., $Al_{0.45}Ga_{0.55}As$ instead of $Al_{0.33}Ga_{0.67}As$. Although the population inversion and the gain are expected to be similar for both QCLs, the lasers with the higher barriers show smaller threshold current densities as well as higher maximum operating temperatures. This improvement is in part attributed to a reduction of the leakage currents. Another attempt by Indjin *et al.*[9] consisted in the implementation of a double phonon resonance using two intersubband transitions in the gain region that are resonant with the longitudinal optical (LO) phonon in order to improve the population inversion as well as the temperature behavior. So far, however, this approach has not been very successful. In contrast, the highest operating temperatures for GaAs/(Al,Ga)As QCLs have been achieved by Pflügl *et al.*[10] using the so-called bound-to-continuum design. Since a rather small gain is expected for this design, we conjecture that the lower operating field strength F_{op} (30 and 40 kV/cm for the two proposed structures in Ref. 10) is possibly responsible for smaller leakage currents and, therefore, reduced threshold current densities.

The rather large range of values for the lasing energy and threshold current density for nominally identical structures, which has not yet been understood, as well as possible electric-field-dependent leakage currents led us to carry out a comprehensive analysis of a series of GaAs/$Al_{0.45}Ga_{0.55}As$ QCLs. For this analysis, we calculate the (quasi-) gain of the respective structures as a function of the transition energies and the electric field strength for a large number of data points (energy and field strength). We self-consistently solve the Schrödinger and Poisson equations using a transport model on the basis of a system of scattering-rate equations and correlate the calculated gain values with the measured threshold current densities. The focus of this study on the internal processes of midinfrared QCLs based on the GaAs/(Al,Ga)As materials system may also be useful for the understanding of terahertz lasers, for which this materials system is the preferred one. Furthermore, there may be still a significant potential for improvements of midinfrared

[a]Electronic mail: lutz@pdi-berlin.de

GaAs/(Al,Ga)As QCLs, if leakage currents can be reduced, although (In,Ga)As/(In,Al)As QCLs on InP substrates appear to be superior in this spectral range with respect to threshold current densities as well as temperature behavior. Finally, the larger flexibility with respect to barrier heights by just manipulating the Al content without introducing strain to the layer system simplifies systematic investigations in this system.

II. THEORETICAL MODEL

The calculation is based on the Schrödinger equation in the envelope function approximation. In order to incorporate the nonparabolicity of the band structure, an effective mass, which depends linearly on the energy, is introduced.[11] This leads to a quasi-$\mathbf{k}\cdot\mathbf{p}$ model with two bands,

$$\begin{pmatrix} V_s(z)+V_{\mathrm{el}}(z) & i\hbar(1/\sqrt{2m_0\gamma})(\partial/\partial z) \\ i\hbar(1/\sqrt{2m_0\gamma})(\partial/\partial z) & -\mu_0(z)/\gamma+V_{\mathrm{el}}(z) \end{pmatrix}\begin{pmatrix}\psi_1(z)\\ \psi_2(z)\end{pmatrix} = E\begin{pmatrix}\psi_1(z)\\ \psi_2(z)\end{pmatrix}, \tag{1}$$

with $V_s(z)$ denoting the conduction band discontinuity determined by the materials, m_0 the free electron mass, $\mu_0(z)$ the effective mass for vanishing momentum in units of the free electron mass, γ the so-called nonparabolicity parameter in units of the free electron mass per meV, $V_{\mathrm{el}}(z)$ the electric potential created by both the external electric field and the internal space charge distribution, $\psi_{1,2}(z)$ the wave functions corresponding to the two bands, E the energy, and $\hbar$ Planck's constant. The eigenvalue problem is solved numerically either by means of the finite-element method or of Fourier series using standard numerical routines. For the self-consistent procedure, the corrections of the potential are calculated from the charge distribution $\rho(z)$ using the Poisson equation in the form

$$\frac{\partial^2}{\partial z^2}V_{\mathrm{el}}^{\mathrm{corr}}(z)=\frac{1}{\varepsilon\varepsilon_0}\rho(z), \tag{2}$$

with periodic boundary conditions. $\varepsilon=12.5$ and ε_0 denote the average dielectric constant of the heterostructure and the vacuum permittivity, respectively. The charge distribution is determined in the framework of a simple rate equation model. For this calculation, the heterostructure is assumed to be infinite, and all periods of the structure are equal. Note, however, that a single period already consists of a large number of layers. In order to reduce the computation effort, the k-space integration in the layer plane is neglected, and the transport is described using scattering rates, which are assumed to be proportional to the corresponding dipole matrix element D_{ij} for a respective pair of states. We use $D_{ij}=\langle\psi^{(j)}|\mathcal{Z}|\psi^{(i)}\rangle$ with

$$|\psi^{(i),(j)}\rangle=\begin{pmatrix}\psi_1^{(i),(j)}\\ \psi_2^{(i),(j)}\end{pmatrix} \text{ and } \mathcal{Z}=\begin{pmatrix}z & 0\\ 0 & z\end{pmatrix},$$

similar to Ref. 12. In addition to the resonant coupling of states, LO-phonon scattering and, in particular, its onset are expected to have an important impact on the transport properties. In order to simulate the in-plane k-space integration, the rates T_{ij} are assumed to depend on the transition energies $\Delta E=E_i-E_j$ so that we use $T_{ij}=\tau(\Delta E)|D_{ij}|^2$ with an energy-dependent factor $\tau(\Delta E)$ for the numerical simulation. LO-phonon scattering is simulated by a steplike increase of $\tau(\Delta E)$ for energies around $E_{\mathrm{LO}}=36$ meV with a superposition of a Lorentzian line shape. For activation, an exponentially decaying contribution is added. Interface roughness is considered by a convolution of the resulting quasistep functions with a Gaussian distribution function. For the numerical analysis, we use

$$\tau(\Delta E)=\frac{1}{2}\left\{\exp\left(\frac{\Delta E}{E_a}+\frac{\sigma^2}{2E_a^2}\right)\left[1-\Phi\left(\frac{\Delta E}{\sqrt{2}\sigma}+\frac{\sigma}{\sqrt{2}E_a}\right)\right]+1+\Phi\left(\frac{\Delta E}{\sqrt{2}\sigma}\right)\right\}\times\left\{1+\kappa_{\mathrm{LO}}\left[1+\Phi\left(\frac{\Delta E-E_{\mathrm{LO}}}{\sigma_s}\right)+E_0\frac{\Gamma}{(\Delta E-E_{\mathrm{LO}})^2+\Gamma^2}\right]\right\}, \tag{3}$$

with the following parameters: $E_a=3$ meV, $\sigma=5$ meV, $\Gamma=5$ meV, and $E_0=1$ meV to simulate thermal activation, interface roughness, broadening, and strength of the LO-phonon resonance, respectively. Furthermore, $\sigma_s=3$ meV and $\kappa_{\mathrm{LO}}=25$ denote the width and strength of the steplike increase of $\tau(\Delta E)$ at the LO-phonon resonance, respectively, and $\Phi(x)$ the error function.

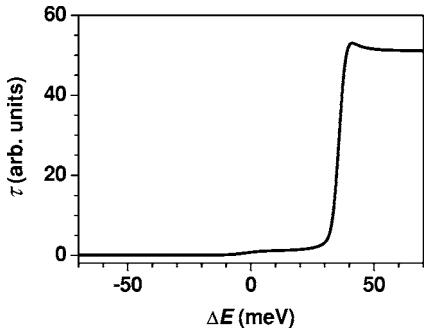

FIG. 1. Energy-dependent factor τ as a function of the transition energy ΔE.

For the parameters listed in the previous paragraph, τ is shown as a function of ΔE in Fig. 1. Assuming a dipole matrix element of 2.5 nm for a 10-nm-wide $GaAs/Al_{0.45}Ga_{0.55}As$ quantum well, a scaling factor of 0.003 $ps^{-1}\,nm^{-2}$ leads to a scattering rate of about 1 ps^{-1} for energies above 36 meV, while for lower energies (acoustic phonons) the rate is about two orders of magnitude smaller, which corresponds roughly to experimental results reported, e.g., by Faist *et al.*[13] The actual values of the scattering rates are mainly determined by κ_{LO}, E_0, and Γ. The latter parameter was introduced in order to be able to simulate scattering effects at larger in-plane wave vectors and is still somewhat random. E_0 and σ are of minor importance for the investigated structures as they modify $\tau(\Delta E)$ only for energies below the LO-phonon energy. Since the experiments were carried out at low temperatures, E_a is set to 3 meV, which corresponds to about 35 K, although the actual electron temperature is expected to be larger. The value of 5 meV for σ was chosen to simulate thickness fluctuations of a few monolayers for 5- to 10-nm thick quantum wells.

The rate equation system for the total occupation numbers N_i of the ith subband in the stationary case as given by

$$\frac{dN_i}{dt} = 0 = \sum_j (T_{ji}N_j - T_{ij}N_i) \tag{4}$$

accounts for all states below the barrier band edge as well as transitions from/to the adjacent periods. Finally, we obtain

$$\rho(z) = \rho_D(z) + e\sum_i N_i|\psi_i(z)|^2, \tag{5}$$

with $\rho_D(z)$ denoting the doping profile and e the electron charge.

As a measure for the gain/loss at the energy of a particular transition, we use $\tilde{G}=(N_i-N_j)|D_{ij}|^2$. In order to correlate the gain with the threshold current density, we define also the (quasi-) gain coefficient by the ratio of the gain and the current density $\tilde{g}=\tilde{G}/j$. For the current density j, we sum over all carrier transitions of one period into the next one through any interface determined by the product of the transition rate and the population of the respective initial state,

$$j = \sum_{i,j} N_i T_{ij}. \tag{6}$$

While the transition energies can be calculated in meV, our model leads only to values for $\tilde{g}$, $\tilde{G}$, and j in arbitrary units. The calculated *gain spectra* consist of a set of discrete *gain values* $\tilde{G}$ for the respective transition energies without a finite line width. This approach is, however, sufficient for a comparison of different structures with respect to the threshold current density. Its significant advantage is the reduced computation effort so that a large range of electric field strengths can be covered with a relatively high resolution.

The self-consistent iteration procedure can become unstable, in particular, for higher carrier concentrations. In order to approach the fixed point, the potential corrections $\Delta V_{\mathrm{el}}^{(l)}(z)$ are adjusted in each step l by a convergence factor κ_l, which lies in the range between 0 and 1. Accelerated iteration is usually achieved using a self-adjusting κ_l that accounts for the magnitude of $\Delta V_{\mathrm{el}}^{(l)}(z)$ or using perturbation iteration methods.[14] However, due to multiple resonant coupling effects in the subband system, even minor potential corrections may lead to significant modifications of the subband structure and consequently to a large $\Delta V_{\mathrm{el}}^{(l+1)}(z)$ for the next step. Therefore, the following, rather intuitive procedure is used for the adjustment of κ_l. Considering the functions $\Delta V_{\mathrm{el}}^{(l)}(z)$ as elements of the Hilbert space of real functions $f(z)$ and $g(z)$ with the scalar product $\langle f(z)|g(z)\rangle = \int f(z)g(z)dz$, an angle α between the two last corrections $\Delta V_{\mathrm{el}}^{(l)}$ and $\Delta V_{\mathrm{el}}^{(l-1)}$ can be determined according to

$$C_{l,l-1} = \cos\alpha = \frac{\langle \Delta V_{\mathrm{el}}^{(l)}(z)|\Delta V_{\mathrm{el}}^{(l-1)}(z)\rangle}{\|\Delta V_{\mathrm{el}}^{(l)}\|\|\Delta V_{\mathrm{el}}^{(l-1)}\|}, \tag{7}$$

where $\|f(z)\| = \sqrt{\langle f(z)|f(z)\rangle}$. If $\alpha=0$ ($C_{l,l-1}=1$), the correction proceeds in the same direction as in the step before so that κ_l should be enlarged, while in the opposite case ($\alpha=180°$, i.e., $C_{l,l-1}=-1$) κ_l should be reduced. It was empirically found that the convergence is improved if this factor is modified according to

$$\kappa_l = \kappa_{l-1}(0.9 + 0.6C_{l,l-1}), \tag{8}$$

starting the algorithm with $\kappa_1=1$. Furthermore, while a larger number of nodes in the finite elements or larger number of Fourier coefficients stabilize the iteration, the calculation time for each step increases significantly. Therefore, an optimum has to be found, which may depend on the parameters (number of layers and carrier concentration) of the structure to be calculated.

III. EXPERIMENTAL DETAILS

We investigate a set of GaAs/$Al_xGa_{1-x}As$ QCLs following the designs by Page *et al.*[8] (sample A), Indjin *et al.*[9] (sample B), and Pflügl *et al.*[10] (sample C, corresponding to sample S1 of Ref. 10). The samples were grown by molecular-beam epitaxy on GaAs(100) substrates. The plasmon-assisted waveguides[7] consist of a stack of a 4-μm-thick GaAs layer Si-doped with 4×10^{16} cm^{-3} and a 1-μm-thick GaAs layer Si-doped with 4×10^{18} cm^{-3} on either side for samples A and B, while the thicknesses of the corresponding GaAs layers are modified to 3.2 and 1.4 μm for sample C. The actual layer thicknesses for the cascade structure and the actual Al content x of the barriers, which we use for the calculations, were obtained from a comparison of the experimental (002) and (004) x-ray diffraction curves, respectively, with simulations. For sample A, we used the following layer thicknesses in nanometers starting with the injection barrier (bold: barrier and underlined: doped), **4.6**, 1.8, **1.1**, 5.18, **1.1**, 4.6, **2.8**, 3.26, **1.7**, 2.88, **1.8**, 2.69, **2.0**, 2.88, **2.6**, and 2.88, with $x=0.49$ and a nominal sheet doping density $n_{2D}=3.9\times10^{11}$ cm^{-2}/period. For sample B, we used **4.04**, 1.12, **0.58**, 5.6, **0.87**, 5.04, **0.87**, 5.04, **2.89**, 3.64, **1.73**, 3.08, **1.73**, 2.8, **2.02**, 3.08, **2.6**, and 2.8, with $x=0.47$ and $n_{2D}=3.9\times10^{11}$ cm^{-2}/period. The layer sequence of sample C consists of **3.9**, 1.6, **0.94**, 5.4, **0.94**, 5.0, **0.94**, 4.3, **1.9**, 3.5, **2.0**, 3.2, **2.0**, 3.0, **2.2**, 2.9, **2.2**, 2.9, **2.4**, 2.9, **2.7**, 2.9, **2.9**, 2.8, **3.1**, and 2.6, with $x=0.45$ and $n_{2D}=5.6\times10^{11}$ cm^{-2}/period. The corresponding lasers contained 36 periods for sample A, 33 periods for sample B, and 50 periods for sample C. The typical size of the laser stripes, which were prepared by plasma etching, is 19 μm$\times$3.2 mm. The laser emission was studied using pulse-mode operation with a width of 100 ns and a repetition rate of 5 kHz. The infrared spectra were recorded at 7 K for a current density just above the threshold current density j_{th} using a Fourier-transform spectrometer (Bruker IFS 66v) with a spectral resolution of 0.12 cm^{-1}.

IV. RESULTS AND DISCUSSION

We calculated the gain spectra for electric field strengths between 30 and 80 (10 and 70) kV/cm for samples A and B (sample C) with a step width of 0.2 kV/cm using a conduction band discontinuity of $V_s(x)=982x$ meV and an effective mass of $\mu_0(x)=0.067+0.083x$ for an Al content x. The nonparabolicity parameter γ was set to 4×10^{-5} meV^{-1}. For the presentation of the dependence of the gain on energy ΔE and electric field strength F, we divided the energy range from

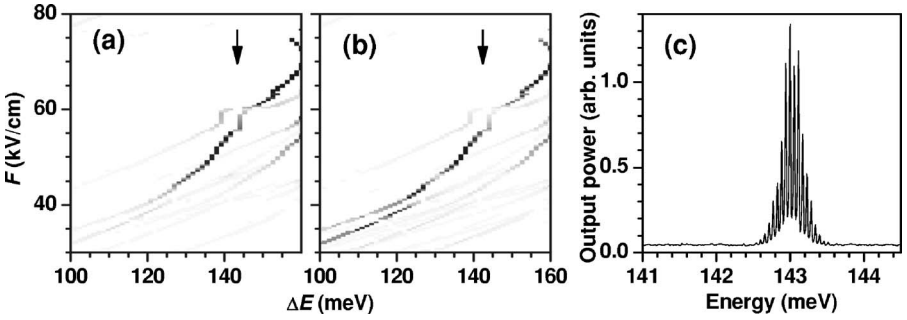

FIG. 2. (a) Gain value $\tilde{G}$ and (b) gain coefficient $\tilde{g}$ for sample A as a function of transition energy ΔE and electric field strength F in a gray-scale representation. White areas correspond to regions with gain values smaller or equal to zero, while black areas indicate values of $\tilde{G}$ and $\tilde{g}$ larger than 5 and 80, respectively. The arrows indicate the lasing energy. (c) Laser spectrum for sample A at a temperature of 7 K operating just above the threshold current density.

100 to 160 meV into intervals of 0.6 meV, added all gain values with energies belonging to a certain interval, and allocated the sum to the center energy of this interval. Negative values for $\tilde{G}$, which correspond to transitions between subbands without population inversion, indicate a possible reabsorption and could, therefore, reduce a positive gain in adjacent intervals. Since the energies and field strengths of negative gain are clearly separated from areas with positive gain for all structures that have been analyzed, negative gain values are not considered in the following discussion.

Figure 2(a) shows a gray-scale plot of the positive gain $\tilde{G}$ for sample A. Note that the characteristics exhibit only sharp lines rather than a smooth, two-dimensional landscape, since we calculate only transitions between states neglecting the line width due to the in-plane band structure. Considerable gain is obtained for a large range of energies (130–160 meV) and electric field strengths (45–70 kV/cm) with maxima at 140 meV (55 kV/cm) and at 155 meV (67 kV/cm). A similar behavior is observed for the gain coefficient $\tilde{g}$ except for an additional maximum at 128 meV (44 kV/cm) as shown in Fig. 2(b). The emission spectrum of sample A taken at an electric field strength of about 54 kV/cm reveals a lasing energy of 143 meV as shown in Fig. 2(c). The values for the lasing energy and the electric field strength are very close to the second gain maximum at about 55 kV/cm with $\tilde{G}=5$ and $\tilde{g}=60$. While the maximum at about 67 kV/cm is correlated with the alignment of the ground state in the injector and the upper laser level, the maximum at 55 kV/cm is due to the coupling of the second injector state with the upper laser level. Figure 3 shows the subband structure of sample A for this field strength. We conclude that this QCL operates at the coupling of the second injector level with the upper laser level rather than at the designed conditions, although the calculated values for $\tilde{G}$ and $\tilde{g}$ are higher there. A possible explanation is that leakage currents may be rather large at the designed field strength. Furthermore, the rather wide gain range provides a more convincing possibility to explain the large fluctuations of the lasing energy than the discussion in Ref. 4 of the possible effect of the splitting of the laser level in $GaAs/Al_{0.33}Ga_{0.67}As$ QCLs due to the strong coupling with the injector. The wide range of field strengths with a gain value that can compensate the optical losses provides a wide range of possible lasing energies. However, we have observed that the emission energy of lasers processed from the same piece of the wafer in the same run varies very little. Even if operated at different current levels, i.e., electric field strengths, the lasing energy appears to be pinned. This behavior is not yet understood.

A similar result is obtained for $\tilde{G}$ and $\tilde{g}$ of sample B as shown in Figs. 4(a) and 4(b), respectively. For this structure, the calculated values for $\tilde{G}$ are larger than the ones for sample A, while the values of $\tilde{g}$ are smaller. The emission spectrum of sample B taken at an electric field strength of about 43 kV/cm reveals a lasing energy of 119 meV as shown in Fig. 4(c). For this lasing energy, we obtain $\tilde{G}=10$ and $\tilde{g}=40$. The threshold current density for this QCL (4.2 kA/cm^2) is larger than the value for sample A (2.9 kA/cm^2). The field strength taken from the gain characteristics of 50 kV/cm is somewhat larger than the measured one.

Sample C is different from the other two insofar as the designed operating field strength is 40 kV/cm, and the period of the cascade structure is longer. Furthermore, the number of periods is increased from 36 to 50. As shown in Figs. 5(a) and 5(b), the shape of the gain curves is clearly different from the ones for samples A and B. The emission spectrum of sample C taken at an electric field strength of about 36 kV/cm reveals a lasing energy of 114 meV as shown in Fig. 5(c). For this lasing energy, the gain value $\tilde{G}$ (about 4.5) as well as the gain coefficient $\tilde{g}$ (about 22) are significantly

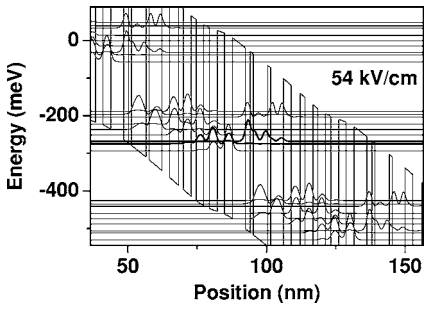

FIG. 3. Part of the conduction band profile and the subband structures for sample A at a field strength of 54 kV/cm, at which the second injector level resonantly couples to the upper laser level. The thick solid lines depict the wave functions of theses two states.

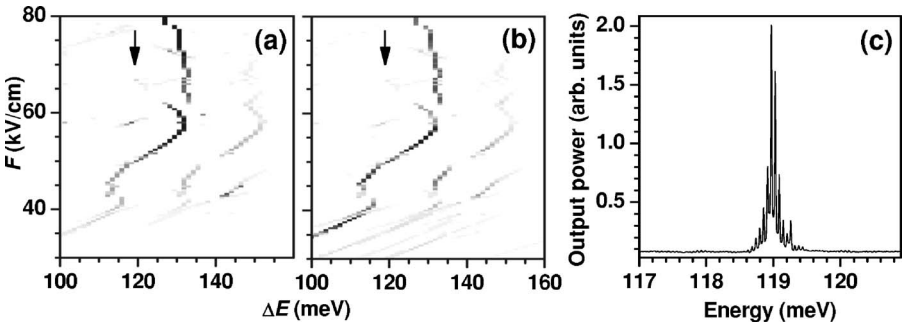

FIG. 4. (a) Gain value $\tilde{G}$ and (b) gain coefficient $\tilde{g}$ for sample B as a function of transition energy ΔE and electric field strength F in a gray-scale representation. White areas correspond to regions with gain values smaller or equal to zero, while black areas indicate values of $\tilde{G}$ and $\tilde{g}$ larger than 20 and 60, respectively. The arrows indicate the lasing energy. (c) Laser spectrum for sample B at a temperature of 7 K operating just above the threshold current density.

smaller than the respective values for samples A and B. Nevertheless, the threshold current density (5.2 kA/cm^2) is only slightly higher than the one of sample B. Note that this value is even smaller than the threshold current density reported in Ref. 10. However, the most striking effect is that this sample exhibits the highest maximum operating temperature of all $GaAs/Al_{0.45}Ga_{0.55}As$ QCLs that we have investigated. Again, this behavior is believed to be due to the smaller operating field strength of about 40 kV/cm as taken from Fig. 5(a) at the lasing energy, which is close to the measured one.

In order to verify these results, we also investigated a series of six additional samples, which are based on the design of sample A, but show some intentional as well as unintentional deviations from the nominal layer structure. In the same way as for samples A–C, the actual layer sequence and Al content of the barriers were determined by x-ray diffractometry. The gain characteristics were calculated, from which the corresponding values for $\tilde{g}$ and the electric field strength were taken at the measured lasing energy. In those cases, in which there is no pronounced gain maximum at the lasing energy, we used the data point with $\tilde{G}=5$ closest to the experimental value for the lasing energy. The absence of a pronounced gain maximum at the lasing energy can be explained by an experimental error for the Al content, since even a small variation of this value may significantly shift the gain characteristics.

Assuming the same resonator properties for all samples, in particular, neglecting the influence of the lasing energy on the waveguide losses as discussed in Ref. 15, the product of the (measured) threshold current density j_{th} and the (calculated) gain coefficient $\tilde{g}$ is expected to be the same for all samples. Figure 6 shows the value for $\tilde{g}j_{th}$ as a function of the derived operating field strength F_{op}. There is a clear increase of this value with increasing field strength. We conclude that the losses increase with increasing field strength. Since the optical (external) losses can be assumed to be independent of the field strength, this result implies that the internal losses significantly increase with increasing field strength between 40 and 60 kV/cm. We believe that such losses can be related to the so-called leakage currents, which are not incorporated in our transport model. These leakage currents can result from scattering of electrons into quasicontinuum states above the barrier. This process becomes more probable as the field strength increases. An additional leakage current can be caused by scattering into defect states. Both the quasicontinuum states and defect states do not contribute to the calculated current in our model, since only a limited number of subbands below the barrier band edge is taken into account. All other contributions to the current due to intersubband transitions, which may or may not affect the gain value, are included.

Note that the significance for the value of $\tilde{g}j_{th}$ for sample C must not be overestimated, since this sample has a different resonator structure and a larger number of periods than samples A and B. Therefore, this sample may exhibit different optical losses than the other ones. Nevertheless, QCLs operating at lower field strengths (around 40 kV/cm) seem

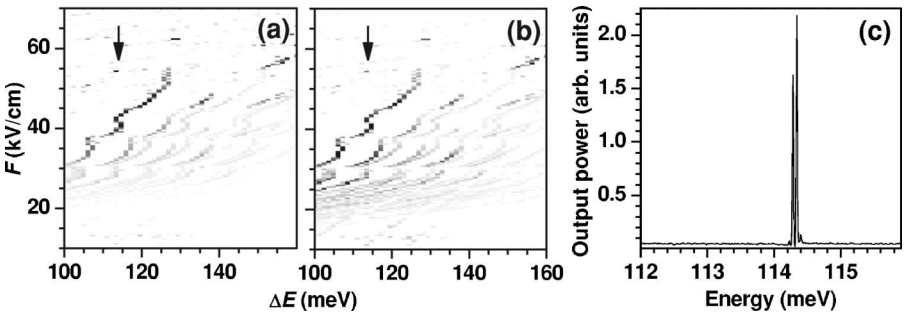

FIG. 5. (a) Gain value $\tilde{G}$ and (b) gain coefficient $\tilde{g}$ for sample C as a function of transition energy ΔE and electric field strength F in a gray-scale representation. White areas correspond to regions with gain values smaller or equal to zero, while black areas indicate values of $\tilde{G}$ and $\tilde{g}$ larger than 5 and 20, respectively. The arrows indicate the lasing energy. (c) Laser spectrum for sample C at a temperature of 7 K operating just above the threshold current density.

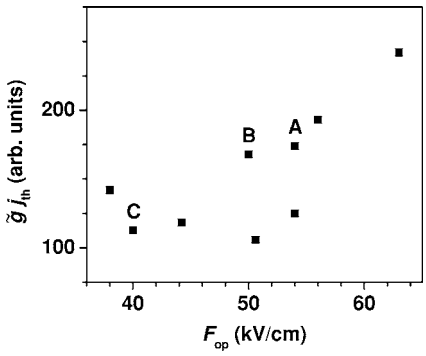

FIG. 6. Product of the calculated gain coefficient $\tilde{g}$ at the measured lasing energy and the measured threshold current density j_{th} as a function of the operating field strength F_{op} for the investigated set of QCLs including samples A–C.

to be superior to the ones operating at higher fields (e.g., 60 kV/cm). This conclusion is confirmed by preliminary results on a QCL designed to operate at $F_{\mathrm{op}}=30$ kV/cm, but with a larger $\tilde{g}$ compared to sample C. This sample exhibits rather low values for j_{th} at 7 K as well as for $\tilde{g}j_{\mathrm{th}}$. However, further investigations are in progress in order to evaluate this approach for an improvement of the operating characteristics of GaAs/(Al,Ga)As QCLs.

V. CONCLUSIONS

The calculations of the gain coefficient of GaAs/(Al,Ga)As QCLs for a wide range of transition energies as well as electric field strengths with a high resolution allow for a systematic analysis of the operating characteristics of QCLs. The calculated gain characteristics using the actual layer parameters rather than the nominal values exhibit several maxima, which may in part explain the observation of different lasing energies for nominally identical structures. Furthermore, the correlation of the gain characteristics with the experimentally obtained lasing energies leads to the conclusion that most of the QCLs operate at lower field strengths than the designed ones. This behavior may be interpreted as a consequence of larger leakage currents at higher field strengths, which are derived from the increasing value of the product of the (calculated) gain coefficient and the (measured) threshold current density with increasing field strength. Therefore, GaAs/(Al,Ga)As QCLs designed for operation at lower field strengths are expected to be superior to QCLs operating at higher field strengths.

ACKNOWLEDGMENTS

The authors would like to thank H. Kostial for sample processing and S. L. Lu for useful discussions.

[1] J. Faist, F. Capasso, D. L. Sivco, C. Sirtori, A. L. Hutchinson, and A. Y. Cho, Science **264**, 553 (1994).
[2] R. Köhler *et al.*, Nature (London) **417**, 156 (2002).
[3] M. Giehler, R. Hey, H. Kostial, S. Cronenberg, T. Ohtsuka, L. Schrottke, and H. T. Grahn, Appl. Phys. Lett. **82**, 671 (2003).
[4] L. Schrottke, R. Hey, and H. T. Grahn, Appl. Phys. Lett. **84**, 4535 (2004).
[5] L. Schrottke, S. L. Lu, R. Hey, M. Giehler, H. Kostial, and H. T. Grahn, J. Appl. Phys. **97**, 123104 (2005).
[6] C. Sirtori, P. Kruck, S. Barbieri, P. Collot, J. Nagle, M. Beck, J. Faist, and U. Oesterle, Appl. Phys. Lett. **73**, 3486 (1998).
[7] C. Sirtori, P. Kruck, S. Barbieri, H. Page, J. Nagle, M. Beck, J. Faist, and U. Oesterle, Appl. Phys. Lett. **75**, 3911 (1999).
[8] H. Page, C. Becker, A. Robertson, G. Glastre, V. Ortiz, and C. Sirtori, Appl. Phys. Lett. **78**, 3529 (2001).
[9] D. Indjin *et al.*, AIP Conf. Proc. **772**, 1565 (2005).
[10] C. Pflügl, W. Schrenk, S. Anders, G. Strasser, C. Becker, C. Sirtori, Y. Bonetti, and A. Muller, Appl. Phys. Lett. **83**, 4698 (2003).
[11] Compare, e. g., G. Bastard, *Wave Mechanics Applied to Semiconductor Heterostructures* (Les Éditions de Physique, Les Ulis, 1988), pp. 83–89.
[12] C. Sirtori, F. Capasso, J. Faist, and S. Scandolo, Phys. Rev. B **50**, 8663 (1994).
[13] J. Faist, F. Capasso, C. Sirtori, D. L. Sivco, A. Y. Cho, L. Pfeiffer, and K. West, Solid-State Electron. **37**, 1273 (1994).
[14] F. Stern, J. Comput. Phys. **6**, 56 (1970).
[15] M. Giehler, H. Kostial, R. Hey, and H. T. Grahn, J. Appl. Phys. **96**, 4755 (2004).